Author(s): Taponen, Anni I.; Ayadi, Awatef; Svahn, Noora; Lahtinen, Manu K.; Rouzières, Mathieu; Clérac, Rodolphe; Tuononen, Heikki M.; Mailman, Aaron

Title: Role of Alkyl Substituent and Solvent on the Structural, Thermal, and Magnetic Properties of Binary Radical Salts of 1,2,3,5-Dithia- or Diselenadiazolyl Cations and the TCNQ Anion

Year: 2022

Version: Published version

Please cite the original version:

Taponen, A. I., Ayadi, A., Svahn, N., Lahtinen, M. K., Rouzières, M., Clérac, R., Tuononen, H. M., & Mailman, A. (2022). Role of Alkyl Substituent and Solvent on the Structural, Thermal, and Magnetic Properties of Binary Radical Salts of 1,2,3,5-Dithia- or Diselenadiazolyl Cations and the TCNQ Anion. Crystal Growth and Design, 22(12), 7110-7122. https://doi.org/10.1021/acs.cgd.2c00795

CRYSTAL GROWTH & DESIGN

pubs.acs.org/crystal

Article

Role of Alkyl Substituent and Solvent on the Structural, Thermal, and Magnetic Properties of Binary Radical Salts of 1,2,3,5-Dithia- or Diselenadiazolyl Cations and the TCNQ Anion

Anni I. Taponen, Awatef Ayadi, Noora Svahn, Manu K. Lahtinen, Mathieu Rouzières, Rodolphe Clérac,* Heikki M. Tuononen,* and Aaron Mailman*

Cite This: https://doi.org/10.1021/acs.cgd.2c00795

Read Online

ACCESS | Metrics & More | Article Recommendations | Supporting Information

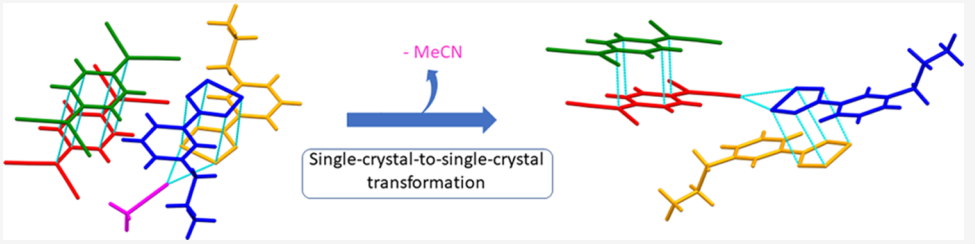

ABSTRACT: The synthesis, structural, thermal, and magnetic properties of a series of simple binary organic salts based on the radical anion of 7,7,8,8-tetracyanoquinodimethane (TCNQ) and 4-(*N*-alkylpyridinium-3-yl)-1,2,3,5-dithiadiazolyl (DTDA), $\mathbf{1}^{R}$ (R = Et, Pr, Bu), radical cations and their heavier selenium analogues (DSDA), $\mathbf{2}^{R}$, are described. Single-crystal X-ray structural analyses reveal that short alkyl substituents on the pyridinium moiety of DTDA/DSDA cations lead to crystallization of isostructural acetonitrile (MeCN) solvates $\mathbf{1}^{Et}$**·MeCN**, $\mathbf{1}^{Pr}$**·MeCN**, $\mathbf{2}^{Et}$**·MeCN**, and $\mathbf{2}^{Pr}$**·MeCN** with *trans*-cofacial DTDA radical cation and eclipsed-cofacial TCNQ radical anion dimers. A slight increase in the substituent chain length to butyl affords the solvate $\mathbf{1}^{Bu}$**·0.5MeCN** or the nonsolvate $\mathbf{1}^{Bu}$. The nonsolvate $\mathbf{1}^{Bu}$ can be exclusively isolated using propionitrile (EtCN), whereas the isostructural selenium analogue $\mathbf{2}^{Bu}$ crystallizes from MeCN. The crystal packing in $\mathbf{1}^{Bu}$**·0.5MeCN** and $\mathbf{1}^{Bu}$/$\mathbf{2}^{Bu}$ is distinctively different: rare one-dimensional (1D) columnar π-stacks of evenly spaced TCNQ radical anions with periodic distortions along the vertical stacking direction and *cis*-cofacial DTDA dimers in $\mathbf{1}^{Bu}$**·0.5MeCN** *vs* discrete, non-eclipsed-cofacial TCNQ dimers and *trans*-antarafacial DTDA/DSDA dimers in $\mathbf{1}^{Bu}$/$\mathbf{2}^{Bu}$. The nonsolvated structure $\mathbf{1}^{Pr}$ with *trans*-cofacial DTDA and non-eclipsed-cofacial TCNQ dimers can be isolated from EtCN. Single-crystal and powder X-ray diffraction methods confirmed a thermally driven, irreversible, single-crystal-to-single-crystal structural transformation between $\mathbf{1}^{Pr}$**·MeCN** and $\mathbf{1}^{Pr}$. Thermogravimetric analyses of all nonsolvated salts show varied, yet robust, thermal behavior, while the thermal behavior of the solvates is consistent with more facile lattice solvent loss from structures with longer *N*-alkyl chains. Variable-temperature magnetic susceptibility measurements indicate that all structures are diamagnetic at low temperatures. However, thermally populated magnetic states could be observed for $\mathbf{1}^{Et}$**·MeCN**, $\mathbf{1}^{Et}$**·EtCN**, $\mathbf{1}^{Pr}$**·MeCN**, $\mathbf{1}^{Bu}$**·0.5MeCN**, $\mathbf{1}^{Bu}$, and $\mathbf{2}^{Bu}$ at higher temperatures. This can be correlated with desolvation and structural changes that lead to the generation of weakly antiferromagnetically coupled non-eclipsed-cofacial TCNQ dimers, in agreement with results from density functional theory (DFT) calculations.

INTRODUCTION

Ion-paired molecular solids containing the ubiquitous electron acceptor 7,7,8,8-tetracyano-*p*-quinodimethane (TCNQ) have been extensively investigated for constituents of new functional materials exhibiting conductive, optical, and/or magnetic properties. A quintessential example of this class of compounds is the 1:1 charge transfer complex between TCNQ and tetrathiafulvalene (TTF), reported in 1973.[1] It was the first example of an organic solid showing metal-like behavior over a large temperature range and maximum electrical conductivity on par with typical metallic elements, such as copper. This system has been intensively explored even to this day, leading to many groundbreaking results. For example, bringing individual crystals of TTF and TCNQ into direct, mechanical contact, a process dubbed crystal laminating, has been found to create stable and reproducible conducting layers with high carrier density without the need of dopants.[2] Recently, nanostructured TTF−TCNQ was found to exhibit excellent electromagnetic performance and electromagnetic interference

Received: July 15, 2022
Revised: September 29, 2022

shielding effectiveness, opening up the possibility to develop electromagnetic response materials based on charge transfer systems.[3]

The TTF−TCNQ charge transfer complex has a unique and well-defined crystal structure in which the formally ionic constituents form alternating and evenly spaced columnar stacks consisting of noneclipsed subunits. As a result, the stacks behave as decoupled, quasi-one-dimensional (1D) electronic systems that lead to the observed conductivity at high temperatures. However, at very low temperatures, the TTF−TCNQ system becomes an insulator owing to two Peierls transitions that occur independently at 38 and 54 K for TTF and TCNQ, respectively.[4] The evenly spaced, uniform columnar packing of $TCNQ^{\cdot-}$ radical anions is relatively uncommon; however, it is observed, for example, in the *N*-methylphenazinium (NMP) salt that also shows high electrical conductivity for an organic species, though several orders of magnitude less than that of TTF−TCNQ.[5,6]

By far the most common packing type in ion-paired TCNQ salts involves the formation of discrete π-dimers of $TCNQ^{\cdot-}$ radical anions with either an eclipsed or noneclipsed geometry (Chart 1). The former geometry typically involves a transversal

Chart 1. Three Most Common Modes of Dimerization for the 7,7′,8,8′-Tetracyanoquinodimethane Radical Anion ($TCNQ^{\cdot-}$)

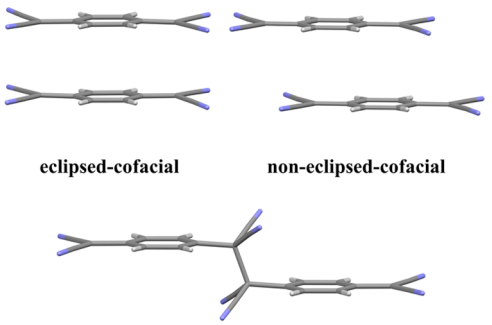

offset of *ca.* 1.0 Å, while the latter is characterized by a longitudinal offset of *ca.* 2.1 Å (Chart 2).[7] In both cases, the unpaired electrons in the dimers are antiferromagnetically coupled *via* strong $\pi-\pi$ interactions, whereas systems with noneclipsed geometry often exhibit thermally accessible triplet states.[8,9] In addition to π-dimerization, $TCNQ^{\cdot-}$ radical anions

Chart 2. Illustration of the Structures of the Binary Salts 1^R and 2^R, and Their Acetonitrile (MeCN) or Propionitrile (EtCN) Solvates, Consisting of a 1,2,3,5-Dithiadiazolyl (DTDA; E = S) or 1,2,3,5-Diselanadiazolyl (DSDA; E = Se) Radical Cation and a TCNQ Radical Anion

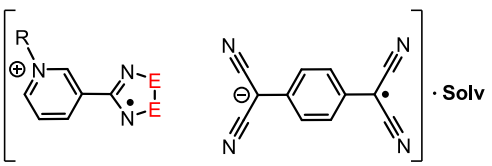

1^R, E = S; 2^R, E = Se
R = Me, Et, Pr, Bu
Solv = MeCN, EtCN

have been found to form σ-dimers in the solid state with long (1.6−1.7 Å) and thereby weak C−C bonds. There are only a dozen structurally characterized examples of σ-dimers of $TCNQ^{\cdot-}$ reported to date,[9−20] with the first example being the *N*-ethylphenazinium (NEP) salt, [NEP][TCNQ].[21] It is striking that such a simple methyl-to-ethyl substitution in the cationic moiety has such a profound influence on the structure of the anion (evenly spaced π-stacks in [NMP][TCNQ] *vs* σ-dimers in [NEP][TCNQ]) and, therefore, to the physical properties of the compound (highly conducting *vs* insulating).

The majority of simple binary salts of the $TCNQ^{\cdot-}$ radical anion contain diamagnetic counter cations, though there are examples of salts with radical cations.[22,23] Recently, we decided to introduce an additional spin to the system by combining $TCNQ^{\cdot-}$ with the 4-(*N*-methylpyridinium-3-yl)-1,2,3,5-dithiadiazolyl radical cation (3-MePyDTDA$^{+\cdot}$) by solution methods to afford the solvates $\mathbf{1^{Me}}$·MeCN and $\mathbf{1^{Me}}$·EtCN, where $\mathbf{1^{Me}}$ = [3-MePyDTDA$^{+\cdot}$][$TCNQ^{\cdot-}$].[24] Such ion-paired salts of molecular radicals can lead to new functional materials with interesting magnetic and/or conductive properties. We showed that the desolvation of $\mathbf{1^{Me}}$·MeCN and $\mathbf{1^{Me}}$·EtCN containing π-dimers of both 3-MePyDTDA$^{+\cdot}$ and $TCNQ^{\cdot-}$ affords the nonsolvate $\mathbf{1^{Me}}$ that, in turn, undergoes a reversible first-order phase transition associated with structural interconversion between two discrete and noninteracting $TCNQ^{\cdot-}$ radicals ($S = 1/2$) and their C−C-bonded σ-dimers ($S = 0$). The magnetic bistability observed for $\mathbf{1^{Me}}$ results from the structural flexibility of the π-dimer of 3-MePyDTDA$^{+\cdot}$ and the intermolecular $S^{\delta+}\cdots N^{\delta-}$ interactions between 3-MePyDTDA$^{+\cdot}$ and $TCNQ^{\cdot-}$ radicals that allow the formation and breakup of the C−C bond in $TCNQ^{\cdot-}$ dimers (1.656(8) Å) without other structural changes.

In this study, we continue our investigations on the radical-ion salts of DTDA$^{+\cdot}$ and $TCNQ^{\cdot-}$ by probing the effect the alkyl chain length on the pyridinium moiety of the DTDA$^{+\cdot}$ radical cation has on the solid-state architecture. As a first approximation, the replacement of the methyl group by a longer alkyl chain is expected to affect the steric properties of the cation alone because the SOMO of DTDA$^{+\cdot}$ is invariant to such substitution. Combined with the pliability of longer alkyl chains, the increased steric repulsion should favor the formation of nonsolvated crystal structures that, in turn, could be advantageous for the formation of σ-dimers of $TCNQ^{\cdot-}$ and possibly new magnetically bistable systems composed of organic radicals. As a further modification to the molecular structure, we performed an atom-to-atom replacement and investigated the behavior of selenium analogues of DTDA$^{+\cdot}$, that is, 4-(*N*-alkylpyridinium-3-yl)-1,2,3,5-diselenadiazolyl radial-cations (DSDA$^{+\cdot}$). The primary motivation for these investigations comes from the well-studied N-alkylphenazinium salts of $TCNQ^{\cdot-}$ discussed above, in which case the identity of the cationic alkyl chain (methyl, ethyl, or butyl) influences not only the $TCNQ^{\cdot-}$ dimerization mode but also the resultant physical properties. Moreover, despite the known role that the cation plays in the solid-state structure and properties of $TCNQ^{\cdot-}$ salts, only a few systematic studies have been reported on the topic to date.

EXPERIMENTAL SECTION

General Methods and Procedures. Full experimental details for the synthesis and characterization of the precursors **I**−**IV** (see Scheme 1) and the salts $\mathbf{1^{Et}}$·MeCN, $\mathbf{1^{Pr}}$·MeCN, $\mathbf{1^{Bu}}$·0.5MeCN, $\mathbf{1^{Et}}$·EtCN, $\mathbf{1^{Pr}}$,

https://doi.org/10.1021/acs.cgd.2c00795
Cryst. Growth Des. XXXX, XXX, XXX−XXX

1^{Bu}, 2^{Et}·MeCN, 2^{Pr}·MeCN, and 2^{Bu} (Scheme 2), are given in the Supporting Information.

Scheme 1. Synthetic Sequence to the Triflate Salts of 4-(*N*-Alkylpyridinium-3-yl)-1,2,3,5-dithiadiazolyl (E = S) and 4-(*N*-Alkylpyridinium-3-yl)-1,2,3,5-diselenadiazolyl (E = Se) Radical Cations, IV[a]

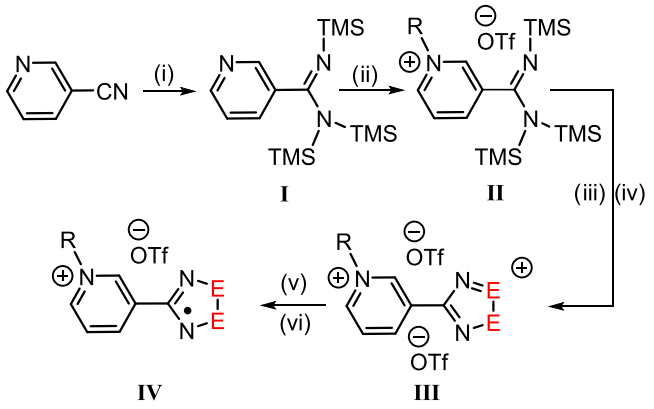

[a]Reagents and general conditions: (i) $LiN(TMS)_2 \cdot Et_2O$, THF, reflux, 16 h, TMSCl; (ii) ROTf, Et_2O, RT, 16 h; (iii) excess S_2Cl_2 or quantitative $SeCl_2$, MeCN, RT, 16 h; (iv) excess TMSOTf, MeCN, RT, 3 h; (v) NBu_4I, MeCN, RT, 3 h; (vi) AgOTf, MeCN, 2 h.

X-ray Crystallography. Variable-temperature single-crystal X-ray diffraction studies were performed on Agilent SuperNova equipped with Atlas CCD detector, dual micro-focus X-ray source (Cu and Mo), and multilayer optics to generate Cu Kα (λ = 1.54184 Å) or Mo Kα (λ = 0.71073 Å) radiation. Crystals were mounted on MiTeGen micro-mounts using Fomblin oil or glass fibers using Wacker silicone paste for low- (<273 K) and high-temperature (>273 K) data collections, respectively. Data acquisitions, reductions, twinning, and analytical face/index-based absorption corrections were made using CrysAlis^{PRO} (v. 39.46).[25] The structures were solved using ShelXT program[26] and refined on F^2 by full-matrix least-squares techniques with the ShelXL program as implemented in Olex (v. 1.2) program package[27] that utilizes the ShelXL-2013 module.[28] C−H hydrogen atoms were calculated to their optimal positions and treated as riding atoms using isotropic displacement parameters 1.2 (aromatic) or 1.5 (aliphatic) times the host atom. Crystallographic data of compounds 1^{Et}·MeCN, 1^{Pr}·MeCN, 1^{Bu}·0.5MeCN, 1^{Et}·EtCN, 1^{Pr}, 1^{Bu}, 2^{Et}·MeCN, 2^{Pr}·MeCN, and 2^{Bu} are compiled in Tables 1 and 2; crystallographic data of derivatives of **IV** are given in the Supporting Information (Tables S1 and S2). In the case of 1^{Bu}·0.5MeCN, poor crystallinity and/or the combination of severe nonmerohedral twinning was persistent across several samples that led to poor data quality. The atom connectivity and crystal packing, however, were clearly established and consistent between two independent data sets. Full crystallographic details are available in the Supporting Information.

Powder X-ray Diffraction. Powder X-ray diffraction measurements were performed on PANalytical X'Pert PRO MPD diffractometer using Cu Kα radiation (λ = 1.5418 Å; 45 kV, 40 mA). In routine experiments, a freshly crystallized and lightly hand-ground powder sample was prepared on zero-background signal generating silicon plate using petrolatum jelly as an adhesive. Diffraction intensities were recorded from spinning samples. In variable-temperature work, a lightly ground sample was placed into an Anton Paar TTK450 temperature-controlled chamber equipped with an automated sample-stage height controller. Diffraction data were acquired by an X'Celerator detector using 2θ ranges of 3−60 and 4−40° in routine and variable-temperature experiments, respectively. A step size of 0.017° and counting times from 60 to 240 s per step were used based on the sample to acquire sufficient diffraction intensities. In variable-temperature measurements, samples were heated/cooled with a heating/cooling rate of 10 K min^{-1} under a nitrogen atmosphere. Each powder pattern was recorded isothermally at the chosen temperature. The diffractometer was aligned using a silicon powder standard material (SRM 640, National Institute of Standards & Technology), and the temperature was calibrated by monitoring the solid-state phase transition of KNO_3 from orthorhombic to trigonal structure (402 K). Data processing and Pawley fits were performed with the program X'Pert HighScore Plus (v. 4.9).[29] The unit cell parameters of the powder samples were refined by Pawley analysis using the corresponding single-crystal structure parameters as the basis of least-squares refinements. Variables used in the fits were zero-offset, polynomial background, sample displacement, and unit cell parameters along with peak profile parameters including peak width, shape, and asymmetry.[30]

Thermogravimetric Analyses (TGA). Thermogravimetric analyses were performed on a PerkinElmer STA 600 simultaneous thermal (TG/DSC) analyzer using open platinum pan under a nitrogen atmosphere (40 mL min^{-1} flow rate) with a heating rate of 10 K min^{-1} over 295−873 K for DTDA and 295−573 K for DSDA variants. Temperature calibration was performed with an indium standard (PerkinElmer, melting point = 429.60 K) and weight calibration by a standard weight of 50.00 mg at room temperature. All samples were freshly prepared and dried *in vacuo* prior to measurements where 3−8 mg of sample was typically used. Recorded TGA data were processed using the Pyris Manager software (v. 13). The desolvation and decomposition temperatures were determined as extrapolated onset values.

Magnetic Susceptibility Measurements. Magnetic measurements were performed on a Quantum Design SQUID MPMS-XL magnetometer housed at the Centre de Recherche Paul Pascal (CRPP) operating at temperatures between 1.8 and 400 K for dc magnetic fields ranging from −7 to 7 T. Measurements were performed on polycrystalline samples 1^{Et}·MeCN, 1^{Et}·EtCN, 1^{Pr}·MeCN, and 1^{Bu}·0.5MeCN, and the nonsolvates 1^{Bu} and 2^{Bu} (21.7, 24.6, 35.1, 24.9, 33.3, and 18.8 mg, respectively) and introduced in a sealed double polyethene/polypropylene bags (3 cm × 0.5 cm × 0.02

Scheme 2. Double-Displacement Reaction between IV and [K(18c6)][TCNQ] Leads to the Radical-Ion Salts $1^{Et,Pr}$·MeCN, 1^{Bu}·0.5MeCN, $2^{Et,Pr}$·MeCN, and 2^{Bu} in MeCN, and 1^{Et}·EtCN and $1^{Pr,Bu}$ in EtCN (1, E = S; 2, E = Se).

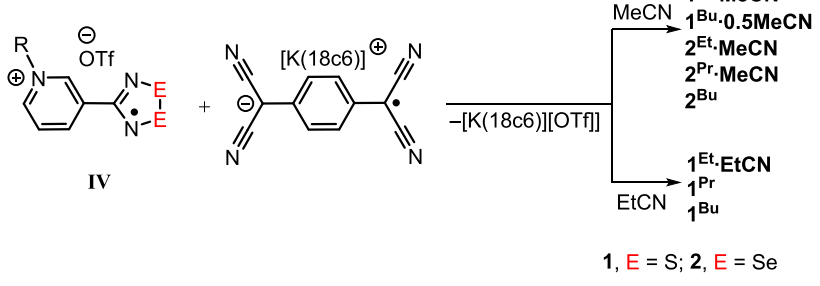

https://doi.org/10.1021/acs.cgd.2c00795
Cryst. Growth Des. XXXX, XXX, XXX−XXX

Table 1. Crystallographic Data for Compounds 1^{Et}·MeCN, 1^{Et}·EtCN, 1^{Pr}·MeCN, 1^{Pr}, 1^{Bu}·0.5MeCN, and 1^{Bu}

	1^{Et}·MeCN	1^{Et}·EtCN	1^{Pr}·MeCN	1^{Pr}	1^{Bu}·0.5MeCN	1^{Bu}
CCDC	2181980	2181982	2181983	2181987	2182780	2181986[b]
formula	$C_{22}H_{16}N_8S_2$	$C_{23}H_{18}N_8S_2$	$C_{23}H_{18}N_8S_2$	$C_{21}H_{15}N_7S_2$	$C_{46}H_{35}N_{15}S_4$	$C_{22}H_{17}N_7S_2$
molecular weight (g mol^{-1})	456.55	470.57	470.59	429.52	926.13	443.54
T (K)	120.00(10)	120.00(10)	120.00(10)	120.00(10)	120.00(10)	120.00(10)
crystal system	triclinic	triclinic	triclinic	triclinic	triclinic	triclinic
space group	$P\bar{1}$	$P\bar{1}$	$P\bar{1}$	$P\bar{1}$	$P\bar{1}$	$P\bar{1}$
a (Å)	8.6768(7)	8.6669(5)	8.8121(5)	8.4212(5)	13.442(3)	6.8439(3)
b (Å)	10.4354(11)	10.4645(6)	10.8960(6)	8.4510(5)	13.464(3)	11.1768(5)
c (Å)	11.9119(10)	13.1169(8)	11.7291(6)	14.1533(8)	13.959(5)	14.2752(7)
α (°)	98.978(8)	74.971(5)	98.130(4)	84.671(5)	92.94(2)	93.617(4)
β (°)	90.426(7)	82.518(5)	92.145(4)	80.088(5)	107.47(3)	90.731(4)
γ (°)	96.364(8)	83.520(4)	97.591(5)	85.166(4)	111.98(2)	106.931(4)
V (Å^3)	1058.46(17)	1135.27(12)	1103.29(11)	985.54(10)	2196.1(11)	1041.99(9)
Z	2	2	2	2	2	2
ρ_{calc} (g cm^{-3})	1.432	1.377	1.416	1.447	1.401	1.414
absorption (μ mm^{-1})	0.280	0.264	0.271	0.295	2.425	0.281
F (000)	472.0	488.0	488.0	444.0	960.0	460.0
2θ range for data collection (deg)	3.978−57.762	4.044−57.77	3.812−57.812	4.852−57.706	6.754−137.994	4.928−57.918
index ranges	$-9 \le h \le 11$ $-14 \le k \le 14$ $-15 \le l \le 14$	$-10 \le h \le 11$ $-13 \le k \le 13$ $-16 \le l \le 17$	$-11 \le h \le 9$ $-14 \le k \le 13$ $-14 \le l \le 13$	$-11 \le h \le 11$ $-11 \le k \le 10$ $-17 \le l \le 19$	$-16 \le h \le 16$ $-16 \le k \le 16$ $-16 \le l \le 16$	$-8 \le h \le 9$ $-14 \le k \le 14$ $-19 \le l \le 18$
reflections collected	7601	8934	8432	12,717	11,546	17,696
independent reflections	4739 [R_{int} = 0.0190, R_{sigma} = 0.0383]	5121 [R_{int} = 0.0226, R_{sigma} = 0.0406]	4941 [R_{int} = 0.0184, R_{sigma} = 0.0361]	4573 [R_{int} = 0.0395, R_{sigma} = 0.0456]	11546 [R_{int} = 0.2257[a], R_{sigma} = 0.1951]	4920 [R_{int} = 0.0279, R_{sigma} = 0.0234]
data/restraints/parameters	4739/0/291	5121/0/300	4941/0/300	4573/0/272	11546/236/492	4920/0/281
goodness-of-fit on F^2	1.047	1.067	1.041	1.085	1.114	1.170
final R indices [$I \ge 2\sigma$ (I)]	R_1 = 0.0366 wR_2 = 0.0861	R_1 = 0.0406 wR_2 = 0.0938	R_1 = 0.0387 wR_2 = 0.0946	R_1 = 0.0526 wR_2 = 0.1602	R_1 = 0.1617 wR_2 = 0.3912	R_1 = 0.0720 wR_2 = 0.1941
final R indices [all data]	R_1 = 0.0464 wR_2 = 0.0922	R_1 = 0.0548 wR_2 = 0.1013	R_1 = 0.0460 wR_2 = 0.1002	R_1 = 0.0659 wR_2 = 0.1710	R_1 = 0.2663 wR_2 = 0.4381	R_1 = 0.0746 wR_2 = 0.1952
$\Delta\rho_{max}/\Delta\rho_{min}$ (e Å^{-3})	0.29/−0.26	0.33/−0.44	0.35/−0.31	0.98/−0.61	2.88/−0.83	0.69/−0.51

[a]Value for R_{int} is determined for the major component of the twin refinement. See the Supporting Information for details. [b]See also CCDC 2181985.

cm; typically 20−40 mg) in a glovebox with a controlled argon atmosphere. Prior to the experiments, the field-dependent magnetization was measured at 100 K on each sample to detect the presence of any bulk ferromagnetic impurity. As expected for paramagnetic or diamagnetic materials, a perfectly linear dependence of the magnetization that extrapolates to zero at zero dc field was systematically observed; the samples appeared to be free of any ferromagnetic impurities. The magnetic susceptibilities were corrected for the sample holder and the intrinsic diamagnetic contributions.

Density Functional Theory. Singlet−triplet gaps were calculated for TCNQ and DTDA dimers using the structural data from low- and high-temperature crystal structures of 1^{Pr} and 1^{Bu}. The calculations were performed with the functionals PBE1PBE-D3BJ[31−36] and LC-ωhPBE[37−40] using def2-TZVP basis sets.[41] The geometries of the dimers were extracted from the solid-state X-ray structures, and the positions of the hydrogen atoms were optimized at the PBE1PBE-D3BJ/def2-TZVP level of theory prior to energy calculations. Broken-symmetry solutions were used for the singlet states while high-spin reference determinants were employed for the triplet states. Two different methods were used as these kinds of calculations are known to be highly sensitive to the choice of density functional. As expected, the singlet−triplet gaps calculated with the two methods differ quantitatively, but the results are in good qualitative agreement with all structural features, notably the separation of the dimers in the solid state, and show that the TCNQ dimers have singlet−triplet gaps that are always smaller than those calculated for the DTDA dimers.

RESULTS AND DISCUSSION

Synthesis. A synthetic route to DTDA radical cation derivatives and the corresponding DSDA congeners,[42] both as their triflate (OTf^-) salts, **IV**, was achieved by modification of our previously reported methodology (Scheme 1).[43] In brief, *N*,*N*,*N*′-tris(trimethylsilyl)-3-pyridineimidamide **I** was readily obtained as a viscous yellow oil that could be purified by fractional vacuum distillation and subsequently alkylated with *N*-alkyl triflates to afford the corresponding *N*-alkylpyridinium triflates,[44] **II**, as moisture-sensitive salts. Cyclocondensation of **II** with sulfur monochloride (S_2Cl_2) or freshly prepared selenium dichloride ($SeCl_2$),[45] followed by subsequent metathesis with trimethylsilyl trifluoromethanesulfonate (TMSOTf), provided access to the double triflate salts **III**. The dications in these salts could be readily reduced to the monocation radicals with tetrabutylammonium iodide and converted to their more soluble triflate salts by subsequent treatment with silver triflate (AgOTf). Repeated recrystalliza-

https://doi.org/10.1021/acs.cgd.2c00795
Cryst. Growth Des. XXXX, XXX, XXX−XXX

Table 2. Crystallographic Data for Compounds 2^{Et}·MeCN, 2^{Pr}·MeCN, and 2^{Bu}

	2^{Et}·MeCN	2^{Pr}·MeCN	2^{Bu}
CCDC	2181981	2181984	2182311
formula	$C_{22}H_{16}N_8Se_2$	$C_{23}H_{18}N_8Se_2$	$C_{22}H_{17}N_7Se_2$
molecular weight (g mol^{-1})	550.35	564.37	537.34
T (K)	120.00(10)	120.00(10)	120.00(10)
crystal system	triclinic	triclinic	triclinic
space group	$P\bar{1}$	$P\bar{1}$	$P\bar{1}$
a (Å)	8.7199(5)	8.8519(5)	6.8553(3)
b (Å)	10.4193(5)	10.8610(7)	11.2539(10)
c (Å)	12.0089(6)	11.8794(7)	14.3128(7)
α (°)	98.783(4)	98.194(5)	94.004(6)
β (°)	90.104(4)	91.479(5)	90.361(4)
γ (°)	96.494(4)	97.549(5)	106.859(6)
V (Å^3)	1071.16(10)	1119.48(12)	1053.77(12)
Z	2	2	2
ρ_{calc} (g cm^{-3})	1.706	1.674	1.694
absorption (μ mm^{-1})	3.480	3.332	4.593
F(000)	544.0	560.0	532.0
2θ range for data collection (deg)	3.982−59.322	3.824−57.768	8.232−153.464
index ranges	$-11 \le h \le 12$	$-11 \le h \le 11$	$-8 \le h \le 6$
	$-13 \le k \le 13$	$-13 \le k \le 10$	$-13 \le k \le 14$
	$-16 \le l \le 16$	$-15 \le l \le 15$	$-18 \le l \le 18$
reflections collected	8141	8194	6856
independent reflections	5162 [R_{int} = 0.0178, R_{sigma} = 0.0313]	5006 [R_{int} = 0.0283, R_{sigma} = 0.0661]	6856 [R_{int} = 0.1026[a], R_{sigma} = 0.0173]
data/restraints/parameters	5162/0/291	5006/0/300	6856/0/282
goodness of fit on F^2	1.077	1.020	1.055
final R indices [$I \ge 2\sigma$ (I)]	R_1 = 0.0293	R_1 = 0.0402	R_1 = 0.0516
	wR_2 = 0.0747	wR_2 = 0.0687	wR_2 = 0.1498
final R indices [all data]	R_1 = 0.0351	R_1 = 0.0693	R_1 = 0.0557
	wR_2 = 0.0778	wR_2 = 0.0777	wR_2 = 0.1532
$\Delta\rho_{max}/\Delta\rho_{min}$ (e Å^{-3})	0.85/−0.73	0.61/−0.54	1.33/−1.22

[a]Value for R_{int} is determined for the major component of the twin refinement.

tion from degassed acetonitrile (MeCN) and/or propionitrile (EtCN) afforded **IV** as analytical pure solids in moderate to high yields (Supporting Information).

A double-displacement reaction between **IV** and the highly soluble salt [K(18c6)][TCNQ], prepared according to literature procedures,[24,46] gave 1:1 salts of *N*-alkylated DTDA/DSDA cations and TCNQ anion ($\mathbf{1}^{R}$, E = S; $\mathbf{2}^{R}$, E = Se; R = Et, Pr, Bu) see (Scheme 2). When the syntheses of **1** and **2** were performed in MeCN, crystalline products $\mathbf{1}^{Et}$·**MeCN**, $\mathbf{1}^{Pr}$·**MeCN**, $\mathbf{2}^{Et}$·**MeCN**, and $\mathbf{2}^{Pr}$·**MeCN** with one solvent molecule per asymmetric unit were obtained. In the case of E = S and R = Bu, the crystalline solvate $\mathbf{1}^{Bu}$·**0.5MeCN** was formed, whereas the corresponding selenium derivative $\mathbf{2}^{Bu}$ crystallized without any lattice solvent molecules. Substitution of MeCN with EtCN in the double-displacement reaction gave the solvate $\mathbf{1}^{Et}$·**EtCN** along with two nonsolvated structures $\mathbf{1}^{Pr}$ and $\mathbf{1}^{Bu}$. Unfortunately, similar reactions of the selenium derivatives of **IV** could not be carried out in EtCN due to solubility issues.

Crystal Structures of the Salts IV. Crystals of triflate salts of the *N*-alkylated radical cations **IV** (E = S, Se; R = Et, Pr, Bu) were obtained from MeCN and structurally characterized by single-crystal X-ray diffraction (Tables S1 and S2, Supporting Information). All salts display strong ion-pairing between the triflate anion and the DTDA/DSDA rings. The DTDA/DSDA radicals adopt a *trans*-cofacial dimerization mode in all cases except for E = S and R = Bu (monoclinic, space group I_2/a), where the rare twisted-cofacial mode was found with the butyl chain in an *anti-anti-anti* conformation that protrudes above the plane of the almost coplanar pyridinium and DTDA rings (Figure 1), which are twisted by ϕ = 4.8° (ϕ is defined as the angle between the mean planes through all nonhydrogen atoms of the pyridinium and DTDA/DSDA rings, respectively). In the case of E = Se and R = Bu derivative (triclinic, space group $P\bar{1}$), the pyridinium and DSDA rings are not coplanar (ϕ = 10.4°), and the butyl chain adopts an *anti*-gauche-*anti* conformation that extends laterally from the pyridinium ring (Figure 1). Despite the two different modes of dimerization found for the derivatives of **IV**, the interplanar separation $\delta_{DTDA/DSDA}$, defined as the centroid-to-centroid distance between the two $-CN_2S_2/-CN_2Se_2$ rings of the dimer, falls into very narrow ranges of 3.05−3.12 and 3.17−3.19 Å for the DTDA and DSDA dimers, respectively. In all structures of **IV**, the dimers adopt a one-dimensional (1D) head-over-tail π-stacking pattern like that found in related triflate salts of *N*-methylpyridinium-DTDA derivatives.[43]

Crystal Structures of Ethyl Derivatives $\mathbf{1}^{Et}$·MeCN, $\mathbf{1}^{Et}$·EtCN, and $\mathbf{2}^{Et}$·MeCN. Compounds $\mathbf{1}^{Et}$·**MeCN**, $\mathbf{1}^{Et}$·**EtCN**, and $\mathbf{2}^{Et}$·**MeCN** crystallize in a triclinic unit cell (space group $P\bar{1}$) and are isostructural with the previously reported methyl derivative $\mathbf{1}^{Me}$·**MeCN**. Their asymmetric unit comprises one DTDA/DSDA cation, one TCNQ anion, and one solvent molecule. The DTDA/DSDA radicals are dimerized in *trans*-cofacial manner, while the TCNQ radicals form eclipsed-cofacial dimers. Together the cations and anions generate repeating $A^+-A^+\cdots B^-\cdots B^-$ stacking motifs (Figure 2). The

https://doi.org/10.1021/acs.cgd.2c00795
Cryst. Growth Des. XXXX, XXX, XXX−XXX

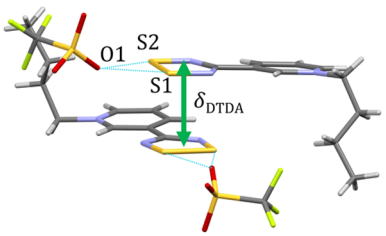

IV (E = S; R = Bu):
δ_{DTDA} = 3.05
S1 ··· O1 = 2.75(1)
S2 ··· O1 = 2.890(8)

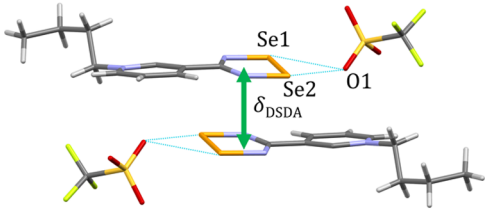

IV (E = Se; R = Bu):
δ_{DSDA} = 3.17
Se1 ··· O1 = 3.014(6)
Se2 ··· O1 = 2.867(7)

Figure 1. Representative view of packing and most important intermolecular interactions in *N*-butyl derivatives of **IV** along with key distances (Å). Minor components of disordered *N*-butyl chains in **IV** (E = S, R = Bu) have been omitted for clarity.

interplanar separation δ_{DTDA} is nearly identical in **1^{Et}·MeCN** and **1^{Et}·EtCN**, 3.15 and 3.16 Å, respectively, and falls within the typical range for *trans*-cofacial DTDA dimers (3.06−3.30 Å) determined from structural data deposited for all DTDA/DSDA radical (or radical cation) derivatives in the Cambridge Structural Database (CSD).[47] The corresponding δ_{DSDA} distance in **2^{Et}·MeCN** is 3.17 Å and, prior to this work, only one structurally characterized example of a DSDA dimer in *trans*-cofacial arrangement had been reported.[48] The centroid-to-centroid distance between two TCNQ radicals, δ_{TCNQ}, is slightly below 3.3 Å in **1^{Et}·MeCN**, **1^{Et}·EtCN**, and **2^{Et}·MeCN**, as is typical for eclipsed-cofacial TCNQ dimers with minor transversal offset (Table S3, Supporting Information). The DTDA/DSDA and pyridinium rings are nearly coplanar (ϕ = 0.9−6.9; Table S3, Supporting Information) in all **1^{Et}·MeCN**, **1^{Et}·EtCN**, and **2^{Et}·MeCN**, which is entirely expected based on existing structural data. Calculations for the phenyl-substituted DTDA radical have shown that ϕ = 0 represents a minimum on the potential energy surface and that even minor perturbations can lead to significant twist angles between the pyridinium and DTDA/DSDA rings.[49] The solvent molecules form supramolecular CN···S/Se interactions with DTDA/DSDA that altogether span a narrow range of 2.888(2)−2.999(2) Å and are significantly shorter than the sum of van der Waals radii for nitrogen and sulfur/selenium atoms (*ca.* 3.35/3.45 Å, respectively). A network of weak C−H···N hydrogen bonds further connects the solvent molecules and DTDA/DSDA cations to TCNQ anions.

Crystal Structures of Propyl Derivatives 1^{Pr}·MeCN, 2^{Pr}·MeCN, and 1^{Pr}. Compounds **1^{Pr}·MeCN** and **2^{Pr}·MeCN** are isostructural with the ethyl derivatives (triclinic unit cell, space group $P\bar{1}$) and contain *trans*-cofacial DTDA/DSDA dimers and eclipsed-cofacial TCNQ dimers forming A$^+$−A$^+$···B$^-$−B$^-$ stacking motifs (Figure 2). The key metrical parameters in **1^{Pr}·MeCN** and **2^{Pr}·MeCN**, such as the centroid-to-centroid distances $\delta_{DTDA/DSDA}$ (3.14 and 3.18 Å, respectively) and δ_{TCNQ} (3.25 and 3.27 Å, respectively) as well as CN···S/Se interactions between solvent molecules and DTDA/DSDA cations (2.897(2)−3.007(4) Å), are all similar to those in **1^{Et}·MeCN**, **1^{Et}·EtCN**, and **2^{Et}·MeCN**.

When the double-displacement reaction between **IV** (E = S; R = Pr) and [K(18c6)][TCNQ] was performed in EtCN, **1^{Pr}** could be crystallized without any solvent molecules in the crystal lattice (Table 1). The crystal structure of **1^{Pr}** (triclinic unit cell, space group $P\bar{1}$) shows DTDA radical cations dimerized in *trans*-cofacial manner (Figure 3). In comparison to the solvate **1^{Pr}·MeCN**, the DTDA and pyridinium rings in **1^{Pr}** are not coplanar and the DTDA rings have slipped further on top of each other, though the δ_{DTDA} distance remains essentially unchanged at 3.11 Å (Table S4, Supporting Information). As in **1^{Pr}·MeCN**, the TCNQ anions form cofacial dimers in **1^{Pr}**, but they adopt a noneclipsed geometry with 2.1 Å longitudinal offset (Table S4, Supporting Information), leading to a significantly increased δ_{TCNQ} distance, 3.73 Å, compared to **1^{Pr}·MeCN**. Overall, the DTDA cations form head-over-tail π-stacks A$^+$−A$^+$···A$^+$−A$^+$ and TCNQ dimers form staircase-like B$^-$−B$^-$···B$^-$−B$^-$ packing motifs in **1^{Pr}** that are connected by supramolecular CN···S

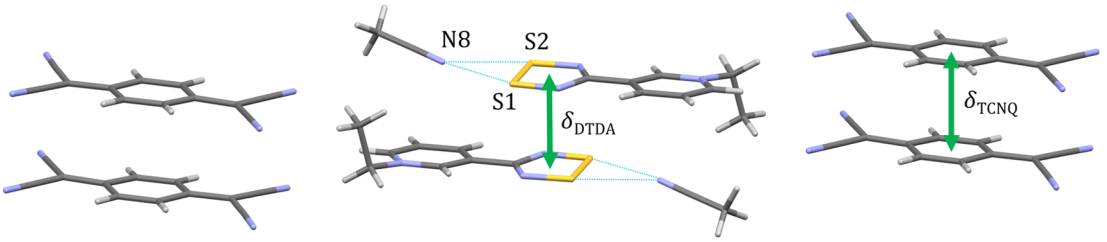

1^{Et}·MeCN:	**1^{Et}·EtCN:**	**2^{Et}·MeCN:**	**1^{Pr}·MeCN:**	**2^{Pr}·MeCN:**
δ_{DTDA} = 3.15	δ_{DTDA} = 3.16	δ_{DSDA} = 3.17	δ_{DTDA} = 3.14	δ_{DSDA} = 3.18
δ_{TCNQ} = 3.26	δ_{TCNQ} = 3.27	δ_{TCNQ} = 3.27	δ_{TCNQ} = 3.25	δ_{TCNQ} = 3.27
S1 ··· N8 = 2.924(2)	S1 ··· N8 = 2.888(2)	Se1 ··· N8 = 2.963(3)	S1 ··· N8 = 2.963(2)	Se1 ··· N8 = 3.007(4)
S2 ··· N8 = 2.914(2)	S2 ··· N8 = 2.906(2)	Se2 ··· N8 = 2.999(2)	S2 ··· N8 = 2.897(2)	Se2 ··· N8 = 2.963(3)

Figure 2. Representative view of packing and most important intermolecular interactions in **1^{Et}·MeCN** and key distances (Å) in the isostructural series **1^{Et}·MeCN**, **1^{Et}·EtCN**, **2^{Et}·MeCN**, **1^{Pr}·MeCN**, and **2^{Pr}·MeCN**.

https://doi.org/10.1021/acs.cgd.2c00795
Cryst. Growth Des. XXXX, XXX, XXX−XXX

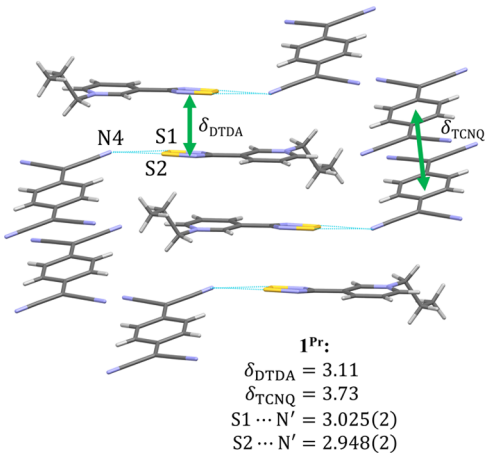

Figure 3. Representative view of packing and most important intermolecular interactions in $\mathbf{1}^{Pr}$ along with key distances (Å).

interactions (2.948(2) and 3.025(2) Å) as well as weak C−H···N hydrogen bonds. The *N*-propyl substituents adopt an *anti-gauche* conformation in $\mathbf{1}^{Pr}$ as opposed to the *anti-anti* conformation found in the solvate $\mathbf{1}^{Pr}$**·MeCN**.

The structure of $\mathbf{1}^{Pr}$ can also be compared to that of $\mathbf{1}^{Me}$ at low temperatures. Even though the solvates $\mathbf{1}^{Me}$**·MeCN** and $\mathbf{1}^{Pr}$**·MeCN** are isostructural, the position adopted by the longer *N*-alkyl chain in the structure of $\mathbf{1}^{Pr}$ and the associated steric effects prevent the formation of C−C-bonded σ-dimers of TCNQ radicals similar to that happens upon desolvation of $\mathbf{1}^{Me}$**·MeCN** to $\mathbf{1}^{Me}$. Hence, $\mathbf{1}^{Pr}$ is not expected to show bistability upon increasing the temperature (*vide infra*).

Crystal Structures of Butyl Derivatives $\mathbf{1}^{Bu}$·0.5MeCN, $\mathbf{1}^{Bu}$, and $\mathbf{2}^{Bu}$. The crystal structure of $\mathbf{1}^{Bu}$**·0.5MeCN** (triclinic unit cell, space group $P\bar{1}$) has two DTDA cations, two TCNQ anions, and only one solvent molecule in the asymmetric unit. The DTDA radicals are arranged in a typical manner to *cis*-cofacial dimers that together form $A^+-A^+\cdots A^+-A^+$ stacks with alternating orientation of the dimeric subunits (Figure 4). The intradimer S···S distances are almost identical, 2.984(7) and

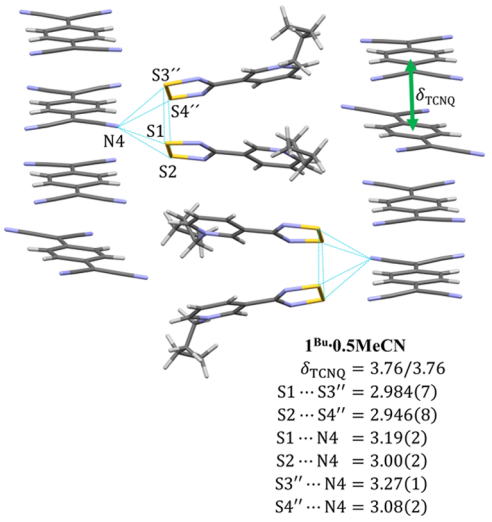

Figure 4. Representative view of packing and most important intermolecular interactions in $\mathbf{1}^{Bu}$**·0.5MeCN** along with key distances (Å). Solvent molecules and disordered *N*-butyl chains have been omitted for clarity.

2.946(8) Å, and within the typical range for *cis*-cofacial DTDA dimers (2.90−3.20 Å) determined from structural data deposited in the CSD.[47] The DTDA dimers in $\mathbf{1}^{Bu}$**·0.5MeCN** are significantly wedged with a tilt angle of 12.2° that arises from the steric demand of the butyl substituents in a lateral *anti*-gauche-*anti* conformation like that found in **IV** (E = Se; R = Bu). The wedged arrangement is not uncommon for DTDA radicals but typically observed in the case of halogenated substituents, such as trifluoromethyl- and fluoro- and chlorophenyls.[50,51] The TCNQ anions form evenly spaced staircase-like $B^-\cdots B^-\cdots B^-$ stacks with two virtually identical δ_{TCNQ} distances, 3.756 and 3.76 Å, and a noneclipsed geometry with 2.0 Å longitudinal offset and negligible transversal offset (Table S4, Supporting Information). However, the neighboring TCNQ radicals are not perfectly aligned but are rotated with respect to each other along the π-stacking direction, with the largest rotational angle observed for every fourth anion (Figure S1, Supporting Information). This creates a rare 1D stacking motif with a periodic distortion of every fourth TCNQ radical anion that results in stacking faults similar to those previously encountered in crown complexes of alkali metal salts of TCNQ.[52] The DTDA and TCNQ stacks are connected by supramolecular CN···S interactions (3.00(2)−3.27(1) Å) as well as weak C−H···N hydrogen bonds. The solvent molecules are embedded in the space between neighboring stacks.

Interestingly, the double-displacement reaction between **IV** (E = Se; R = Bu) and [K(18c6)][TCNQ] in MeCN gave the nonsolvated derivative $\mathbf{2}^{Bu}$. The corresponding sulfur derivative $\mathbf{1}^{Bu}$ could also be synthesized in bulk by performing the analogous double-displacement reaction in EtCN; trace amounts of this product were also formed in MeCN and could be separated from $\mathbf{1}^{Bu}$**·0.5MeCN** based on crystal morphology and characterized by X-ray crystallography.

Compounds $\mathbf{1}^{Bu}$ and $\mathbf{2}^{Bu}$ are isostructural with one DTDA/DSDA cation and one TCNQ anion in the asymmetric unit (triclinic unit cell, space group $P\bar{1}$). The DTDA/DSDA cations are in a rare *trans*-antarafacial arrangement (*trans*-cofacial in $\mathbf{1}^{Pr}$) and form head-over-tail $A^+-A^+\cdots A^+-A^+$ π-stacking motifs (Figure 5). The intradimer S···S distance in $\mathbf{1}^{Bu}$ is 3.172(2) Å and falls to the lower end of the typical range for *trans*-antarafacial DTDA dimers (3.13−3.44 Å) determined from structural data deposited in the CSD. The corresponding Se···Se distance in $\mathbf{2}^{Bu}$ is 3.241(1) Å and is comparable to the data reported for the two other structurally characterized examples of such an arrangement of DSDA radicals (3.215(2)−3.334(2) Å).[48,53] However, this comparison is not entirely warranted because the radicals are charge neutral in all published examples and coordinated to two metal centers in one of the two cases. The twist angle between DTDA/DSDA and pyridinium rings is 22.6 and 23.5° in $\mathbf{1}^{Bu}$ and $\mathbf{2}^{Bu}$, respectively, and thereby significantly greater than in any of the other structures reported. This is presumably due to the weak C−H···N hydrogen-bond network that assembles the TCNQ and pyridinium rings into an almost coplanar arrangement, while simultaneously allowing the DTDA/DSDA cations and TCNQ anions to connect by supramolecular CN···S (2.869(3)Å and 2.962(3) Å) and CN···Se (2.937(5) and 3.017(6) Å) interactions. Like the case of $\mathbf{1}^{Pr}$, the TCNQ dimers adopt a noneclipsed geometry with *ca.* 2.2 Å longitudinal offset and negligible transversal offset (Table S4, Supporting Information). The dimers form staircase-like $B^-\!-\!B^-\cdots B^-\!-\!B^-$ stacks with two vastly differing δ_{TCNQ} distances, 3.70 and 5.18 Å in

https://doi.org/10.1021/acs.cgd.2c00795
Cryst. Growth Des. XXXX, XXX, XXX−XXX

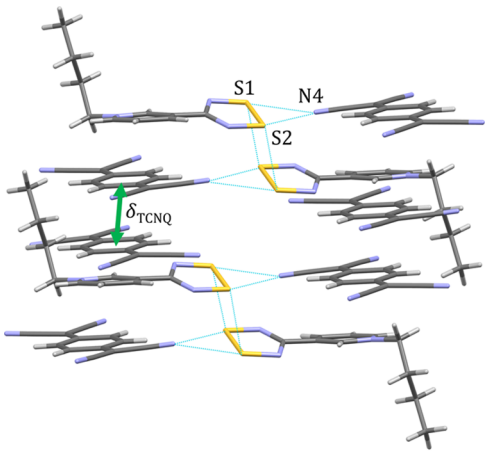

1^{Bu}:	2^{Bu}:
δ_{TCNQ} = 3.70	δ_{TCNQ} = 3.72
S···S = 3.172(2)	Se···Se = 3.241(1)
S1···N4 = 2.962(3)	Se1···N4 = 3.017(6)
S2···N4 = 2.869(3)	Se2···N4 = 2.937(5)

Figure 5. Representative view of packing and most important intermolecular interactions in 1^{Bu} and key distances in isostructural compounds 1^{Bu} and 2^{Bu} (Å).

1^{Bu} and 3.72 and 5.19 Å in 2^{Bu}. The *N*-butyl substituents adopt an *anti-anti-anti* conformation in 1^{Bu} and 2^{Bu}, as opposed to the *anti*-gauche-*anti* conformation found in the solvate **1^{Bu}·0.5MeCN**, preventing the formation of C−C-bonded σ-dimers of TCNQ.

Thermal Behavior of Crystalline Solvates of 1 and 2. The crystallographic data discussed above clearly show the effect of the crystallization solvent and the *N*-alkyl chain length on the dimerization mode of DTDA/DSDA (*cis*-cofacial, *trans*-cofacial, or *trans*-antarafacial) and TCNQ radicals (eclipsed-cofacial or non-eclipsed-cofacial). Interestingly, none of the three nonsolvated structures 1^{Pr}, 1^{Bu}, and 2^{Bu} revealed a σ-dimer of TCNQ akin to the low-temperature (LT) phase of 1^{Me}, indicating that the *N*-methyl substituent plays a role in facilitating the formation of a C−C bond between TCNQ radicals in 1^{Me}. However, it can also be argued that solvent molecules in the crystal lattice of **1^{Me}·MeCN** and **1^{Me}·EtCN** are essential for obtaining the right initial arrangement of cations and anions that then reorganizes upon desolvation to yield the σ-bonded dimer in 1^{Me}. To investigate this further, and to reveal other interesting physical properties for this series of radical-ion salts, the thermal behavior of the solvates **1^{Et}·MeCN**, **1^{Pr}·MeCN**, **1^{Bu}·0.5MeCN**, **1^{Et}·EtCN**, **2^{Et}·MeCN**, and **2^{Pr}·MeCN** was investigated by thermogravimetric analysis (TGA).

The recorded TGA curves allowed the establishment of onset temperatures for the loss of lattice solvent and the %-weight losses calculated from the data were consistent with the stoichiometries established by single-crystal X-ray crystallography (Table S5 and Figures S2−S10, Supporting Information). The variable behavior of the investigated solvates in the release of the solvent, before the onset of decomposition at temperatures >450 K, reflects the varying strength of interactions between solvent molecules and radical ions in the crystal structures of **1^{Et}·MeCN**, **1^{Et}·EtCN**, **1^{Pr}·MeCN**, **1^{Bu}·0.5MeCN**, **2^{Et}·MeCN**, and **2^{Pr}·MeCN** (*vide supra*).

The thermal behavior of the solvates **1^{Et}·MeCN** and **1^{Et}·EtCN** observed in their TGA curves indicated that the solvent is gradually removed from these structures with onset temperatures of 387 and 396 K, respectively. There is only a narrow plateau between the occurrence of desolvation and thermal decomposition at 472 and 452 K for **1^{Et}·MeCN** and **1^{Et}·EtCN**, respectively (Table S5, Figures S2 and S3, Supporting Information). For this reason, we did not attempt a single-crystal-to-single-crystal (SCSC) transformation in these two cases even though the structures contain the shortest *N*-alkyl substituents with the least influence on the packing of TCNQ radicals. The selenium analogue **2^{Et}·MeCN** undergoes a more facile desolvation with an onset temperature of 385 K and decomposition at 452 K. This system was not investigated any further, however, because its *trans*-cofacial DSDA and eclipsed-cofacial TCNQ dimers are strongly

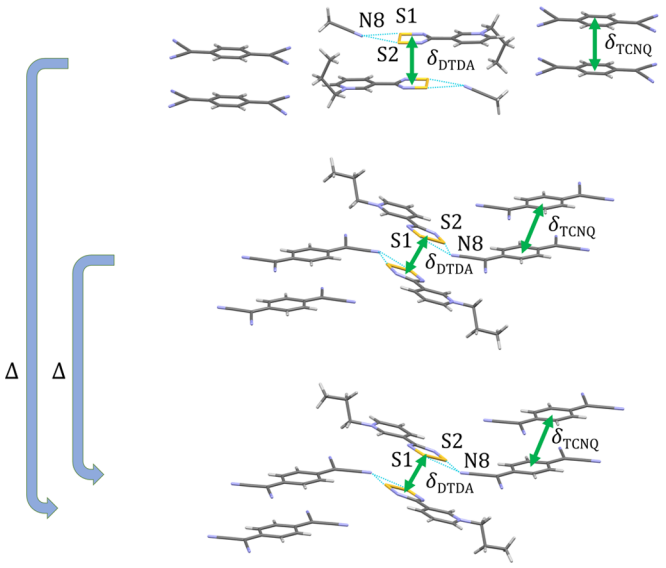

1^{Pr}·MeCN @ 120 K:
δ_{DTDA} = 3.14
δ_{TCNQ} = 3.25
S1···N4 = 2.963(2)
S2···N4 = 2.897(2)

1^{Pr} @ 120 K:
δ_{DTDA} = 3.11
δ_{TCNQ} = 3.73
S1···N4 = 3.025(2)
S2···N4 = 2.948(2)

1^{Pr} @ 370 K:
δ_{DTDA} = 3.21
δ_{TCNQ} = 3.89
S1···N4 = 3.102(9)
S2···N4 = 2.95(1)

Figure 6. Illustration of changes to the solid-state structure of **1^{Pr}·MeCN** upon desolvation to 1^{Pr} and temperature change from 120 to 370 K along with key distances (Å).

https://doi.org/10.1021/acs.cgd.2c00795
Cryst. Growth Des. XXXX, XXX, XXX−XXX

antiferromagnetically coupled, preventing significant changes to both structure and properties upon desolvation.

The two isostructural analogues $\mathbf{1}^{\mathbf{Pr}}$**·MeCN** and $\mathbf{2}^{\mathbf{Pr}}$**·MeCN** displayed a similar behavior in TGA with facile loss of lattice solvent at 354 and 358 K, respectively, and high thermal stability up to >450 K. The robust thermal behavior observed for the salts suggested that an SCSC transformation might be realized in these cases and was attempted for $\mathbf{1}^{\mathbf{Pr}}$**·MeCN**. Again, given the strongly antiferromagnetically coupled *trans*-cofacial DSDA and eclipsed-cofacial TCNQ dimers in $\mathbf{2}^{\mathbf{Pr}}$**·MeCN**, we did not pursue investigations on this system any further.

Careful heating of single crystals of $\mathbf{1}^{\mathbf{Pr}}$**·MeCN** on the goniometer head up to 370 K led to the acquisition of a high-temperature (HT) structure by single-crystal X-ray diffraction that revealed an SCSC transformation to the nonsolvated $\mathbf{1}^{\mathbf{Pr}}$ structure with a triclinic unit cell (space group $P\bar{1}$). The HT crystal structure of $\mathbf{1}^{\mathbf{Pr}}$ is comparable to the LT data discussed above (Table S6, Supporting Information) and shows *trans*-cofacial DTDA dimers and non-eclipsed-cofacial TCNQ dimers with 2.1 Å longitudinal offset and negligible transversal offset (Figure 6). As expected, both δ_{DTDA} and δ_{TCNQ} distances have significantly increased in the HT structure, while the CN···S interactions between cations and anions are much less affected by the change in temperature from 120 to 370 K. The nature of the SCSC transformation observed for $\mathbf{1}^{\mathbf{Pr}}$**·MeCN** effectively confirms that desolvation alone is not sufficient to yield a σ-bonded TCNQ dimer, but the size of the *N*-alkyl substituent plays a key role in the process.

The thermally induced desolvation of $\mathbf{1}^{\mathbf{Pr}}$**·MeCN**, its phase purity, and the associated SCSC transformation to $\mathbf{1}^{\mathbf{Pr}}$ were confirmed in the bulk by variable-temperature powder X-ray diffraction experiments (Tables S7 and S8 and Figures S11–S13, Supporting Information). Subsequent Pawley refinement of the unit cell parameters for each of the powder samples was found to be structurally like the corresponding single-crystal structures. Traces of $\mathbf{1}^{\mathbf{Pr}}$ appear in the bulk of $\mathbf{1}^{\mathbf{Pr}}$**·MeCN** before heating, suggesting that the difference in crystal lattice enthalpy between the solvated and nonsolvated structures is very small. Variable-temperature powder X-ray experiments indicate that the loss of lattice solvent occurs readily above 377 K, with only residual traces of $\mathbf{1}^{\mathbf{Pr}}$**·MeCN** visible in the diffractograms. These results are consistent with the data from TGA (Table S5 and Figure S4, Supporting Information).

In the case of $\mathbf{1}^{\mathbf{Bu}}$**·0.5MeCN**, the solvent molecules in the crystal lattice do not interact strongly with the DTDA radical cation, that is, there are no CN···S interactions in the structure. Instead, the solvent seems to play the role of a space filler in $\mathbf{1}^{\mathbf{Bu}}$**·0.5MeCN**, as indicated by the comparatively low onset temperature for solvent loss at 361 K with decomposition taking place at 457 K (Table S5 and Figure S5, Supporting Information). Unfortunately, the poor quality of single crystals of $\mathbf{1}^{\mathbf{Bu}}$**·0.5MeCN** prevented further investigation of any possible SCSC transformation, but powder X-ray diffraction experiments showed the bulk material to be consistent with the single-crystal structure (Table S7 and Figure S14, Supporting Information).

Both the nonsolvated structures $\mathbf{1}^{\mathbf{Bu}}$ and $\mathbf{2}^{\mathbf{Bu}}$ contain rare *trans*-antarafacial DTDA/DSDA dimers, and Pawley refinement of the unit cell parameters for each of the powder samples was found to be consistent with the corresponding single-crystal structures (Table S8, Figures S15 and S16, Supporting Information). In the case of $\mathbf{1}^{\mathbf{Bu}}$, the nonsolvated material could be obtained from EtCN as sizable single crystals, and an HT single-crystal structure was determined for it at 370 K (Table S6 and Figure S17, Supporting Information). Upon heating, the S···S distance was found to increase significantly from 3.172(2) to 3.312(1) Å, but the value is still within the typical range for DTDA dimers (3.13–3.44 Å). The staircase-like π-stacking of TCNQ dimers along the *a*-axis is maintained in the HT structure of $\mathbf{1}^{\mathbf{Bu}}$, but the δ_{TCNQ} distance has increased from 3.70 to 3.78 Å with very minor changes seen in longitudinal and transversal offsets (Table S4, Supporting Information).

Magnetic Measurements and Computational Investigations. Based on our previous experience with $\mathbf{1}^{\mathbf{Me}}$**·MeCN** and $\mathbf{1}^{\mathbf{Me}}$**·EtCN** that exhibit thermal hysteresis near room temperature due to lattice solvent loss and subsequent first-order phase transition between a paramagnetic HT and a diamagnetic LT phase, the bulk magnetic properties of the solvates $\mathbf{1}^{\mathbf{Et}}$**·MeCN**, $\mathbf{1}^{\mathbf{Et}}$**·EtCN**, $\mathbf{1}^{\mathbf{Pr}}$**·MeCN**, and $\mathbf{1}^{\mathbf{Bu}}$**·0.5MeCN**, and the nonsolvates $\mathbf{1}^{\mathbf{Bu}}$ and $\mathbf{2}^{\mathbf{Bu}}$ were explored. Variable-temperature magnetic susceptibility data using a static field of 1.0 T were collected between 1.85 and 400 K, with different thermal cycling to probe the *in situ* desolvation of the different solvated materials.

All samples are essentially diamagnetic below 300 K, as expected for π-dimers of DTDA and TCNQ radicals with only a very low concentration of spin-defect impurities (Figure 7).

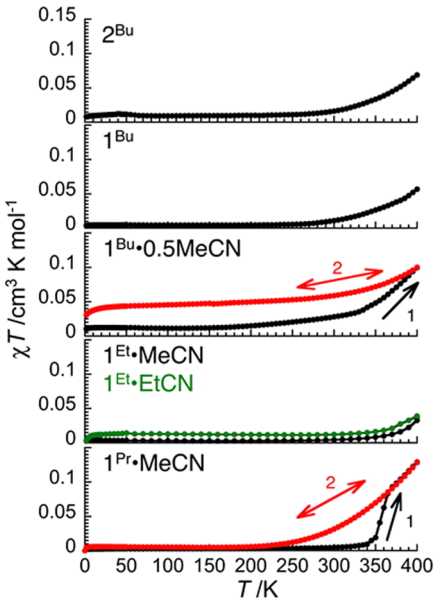

Figure 7. Temperature dependence of the χT product for $\mathbf{1}^{\mathbf{Pr}}$**·MeCN**, $\mathbf{1}^{\mathbf{Et}}$**·MeCN**, $\mathbf{1}^{\mathbf{Et}}$**·EtCN**, $\mathbf{1}^{\mathbf{Bu}}$**·0.5MeCN**, $\mathbf{1}^{\mathbf{Bu}}$, and $\mathbf{2}^{\mathbf{Bu}}$ at 1 T (χ, the *dc* magnetic susceptibility, is defined as M/H per mole of complex).

The solvates $\mathbf{1}^{\mathbf{Et}}$**·MeCN** and $\mathbf{1}^{\mathbf{Et}}$**·EtCN** remained diamagnetic up to 350 K. Above this temperature, only a small increase of the χT product is observed (Figure 7) that is consistent with gradual loss of lattice solvent observed in TGA above 385 K. The magnetic properties upon subsequent cooling from 400 K remain quantitatively unchanged, indicating that solvated and desolvated $\mathbf{1}^{\mathbf{Et}}$ materials possess roughly the same magnetic properties.

In the solvates $\mathbf{1}^{\mathbf{Pr}}$**·MeCN** and $\mathbf{1}^{\mathbf{Bu}}$**·0.5MeCN**, the loss of lattice solvent was evidenced by a steady increase in χT during the first heating cycle with onset temperatures consistent with

https://doi.org/10.1021/acs.cgd.2c00795
Cryst. Growth Des. XXXX, XXX, XXX−XXX

data from TGA (Figures 7, S4 and S5, Supporting Information). A subsequent cooling and heating cycle did not follow the same track of the initial heating. In the case of **1^{Bu}·0.5MeCN**, the loss of lattice solvent led to a small concentration of spin-defect impurities (~10%) that presumably arise from isolated TCNQ radicals within the 1D π-stacks or defect sites generated during desolvation. In the nonsolvated material **1^{Bu}**, a modest thermal population of the excited magnetic states was observed above 300 K. For **1^{Pr}·MeCN**, the maximum value of the χT product, *ca.* 0.15 cm^{3}K mol^{-1}, was recorded at the highest possible temperature of the experiment (400 K, Figure 7). The value is much lower than expected for an ideal $S = 1/2$ system, 0.375 cm^{3}K mol^{-1}. The resulting plot of χT *vs* T plot for **1^{Pr}·MeCN** after loss of lattice solvent is consistent with thermally populated magnetic states above 250 K that, based on the structural data, arise from the weakly interacting noneclipsed TCNQ dimers in **1^{Pr}**. This was probed with DFT using the PBE1PBE and LC-ωhPBE (values reported in parentheses) functionals together with the def2-TZVP basis sets. The calculations revealed a singlet−triplet (S−T) gap of 5 (3) kJ mol^{-1} for the TCNQ dimer in the geometry that it adopts in the HT structure of **1^{Pr}** compared to the S−T gap of 22 (13) kJ mol^{-1} calculated for the DTDA dimer in a similar manner. Corresponding S−T gaps calculated from the LT structure are 12 (8) and 31 (19) kJ mol^{-1} for TCNQ and DTDA, respectively. These values agree with the structural data, that is, the TCNQ radicals are well separated at both temperatures and have small S−T gaps, while the energy gaps calculated for the DTDA radicals are in both cases higher due to δ_{DTDA} being much smaller than δ_{TCNQ} in both structures.

The crystal structures of the isostructural nonsolvates **1^{Bu}** and **2^{Bu}** both showed DTDA/DSDA radicals with a rare *trans*-antarafacial dimerization mode along with non-eclipsed-cofacial TCNQ dimers. The variable-temperature magnetic behavior of **1^{Bu}** and **2^{Bu}** was found to be nearly identical (Figure 7) with thermally populated magnetic states increasing steadily above *ca.* 300 K. The magnetic behavior was found to follow the same track during repeated heating and cooling cycles, as expected based on the available structural data. This magnetic behavior is tentatively attributed to the small S−T gap afforded by the non-eclipsed-cofacial TCNQ dimer geometry at higher temperatures. S−T gaps calculated for TCNQ and DTDA dimers in the geometries they adopt in the HT structure of **1^{Bu}** are 11 (8) and 23 (14) kJ mol^{-1}, respectively. Corresponding values calculated from the LT structure are 19 (13) and 36 (21) kJ mol^{-1} for TCNQ and DTDA, respectively. The calculated values are in accordance with the structural data and show the S−T gaps to be smaller for TCNQ dimers at both temperatures.

CONCLUSIONS

In this work, we have provided a detailed account of the preparation, structural, thermal, and magnetic characterization of a series of simple binary organic radical salts obtained by partnering the ubiquitous 7,7,8,8-tetracyanoquinodimethane radical anion ($TCNQ^{-\cdot}$) with 4-(*N*-alkylpyridinium-3-yl)-1,2,3,5-dithiadiazolyl radical cations ($DTDA^{+\cdot}$) and their selenium analogues ($DSDA^{+\cdot}$).

When using shorter-alkyl-chain substituents ethyl and propyl, the binary salts crystallized as isostructural acetonitrile solvates **1^{Et}·MeCN**, **1^{Pr}·MeCN**, **2^{Et}·MeCN**, and **2^{Pr}·MeCN**. In these structures, the DTDA and DSDA radicals are dimerized in *trans*-cofacial manner and form supramolecular CN···S/Se interactions with the solvent, whereas the TCNQ radicals form eclipsed-cofacial dimers. A slight increase in the alkyl chain length to butyl, however, led to a distinctly different solvate structure **1^{Bu}·0.5MeCN** in which the DTDA radicals form *cis*-cofacial dimers with the solvent molecules settled in the space between butyl substituents while the TCNQ radicals are arranged to a rare 1D columnar stacking motif containing periodic distortions along the vertical stacking direction. Changing the solvent from MeCN to EtCN or replacing sulfur for selenium both favored the isolation of nonsolvated structures in the case of **1^{Pr}**, **1^{Bu}**, and **2^{Bu}**; the solvate **1^{Et}·EtCN** was also obtained. In the nonsolvated structures, the DTDA and DSDA dimers are either in *trans*-cofacial (**1^{Pr}**) or *trans*-antarafacial (**1^{Bu}** and **2^{Bu}**) arrangement, while the TCNQ radicals adopt noneclipsed dimer geometry with substantial longitudinal offset.

The results from this work confirmed our expectation that the steric repulsion and pliability of longer-alkyl-chain substituents on the cation favor the formation of nonsolvated crystal structures. This was found to be particularly true for crystallizations from EtCN that led exclusively to nonsolvates in the case of **1^{Pr}** and **1^{Bu}**; analogous selenium derivatives could not be crystallized from this solvent due to the low solubility of precursor salts **IV** (E = Se, R = Et, Pr, Bu). In all crystal structures containing one solvent molecule per ion, the solvents work as structure-driving agents and arrange the DTDA and DSDA cations to *trans*-cofacial dimers held in place by supramolecular CN···S/Se interactions. Partially solvated and nonsolvated crystal structures show significantly more variation in the arrangement of the ions in the solid state, and there exists no clear structure-driving factor in these cases. Unfortunately, none of the crystal structures obtained in this work revealed the formation of σ-dimers of TCNQ radicals even though **1^{Pr}·MeCN** was found to be isostructural with **1^{Me}·MeCN** and could be thermally desolvated to **1^{Pr}**. Clearly, the *N*-alkyl group in **1^{Pr}** compared to **1^{Me}** is sufficiently bulky to direct the TCNQ radicals to form their most favorable arrangement, non-eclipsed-cofacial dimers, not only in **1^{Pr}** but also in all nonsolvated crystal structures reported in this work.

All nonsolvated salts displayed varied but robust thermal behavior, while the thermal behavior of the solvates revealed a clear trend for the loss of lattice solvent becoming more facile for systems with longer alkyl chains. The thermally induced desolvation of **1^{Pr}·MeCN**, its phase purity, and the associated SCSC transformation to **1^{Pr}** were confirmed in the bulk by variable-temperature powder X-ray diffraction experiments. Variable-temperature magnetic susceptibility measurements showed that all investigated structures are diamagnetic at low temperatures. However, thermally populated paramagnetic states could be observed in all investigated cases above 250 K and, in particular, for the nonsolvated systems **1^{Pr}**, **1^{Bu}**, and **2^{Bu}**. This behavior was tentatively assigned to the noneclipsed geometry of TCNQ radical dimers in these structures that leads to a longer separation between the radical ions at higher temperatures and, consequently, to small singlet−triplet gaps. This interpretation was supported by results from DFT calculations.

Considered as a whole, the systematic investigation of structural and solvent effects on the crystal structure, thermal, and magnetic properties of the simple binary salts **1** and **2** and their solvates has provided structural insight that can be applied to related systems in the design of new functional

https://doi.org/10.1021/acs.cgd.2c00795
Cryst. Growth Des. XXXX, XXX, XXX−XXX

molecular materials. In this context, the selenium analogue of 1^{Me}·MeCN, namely, 2^{Me}·MeCN, appears as an interesting target system. Based on the results reported herein, the S-to-Se atom replacement is not expected to lead to desolvation and the crystal structure of 2^{Me}·MeCN is predicted to be isostructural with 1^{Me}·MeCN. Consequently, 2^{Me} might be a suitable platform to observe σ-dimers of TCNQ radicals in the solid state, possibly leading to bistability like that established in the case of 1^{Me}·MeCN. Synthetic work toward this and related systems are currently underway.

■ ASSOCIATED CONTENT

Supporting Information

The Supporting Information is available free of charge at https://pubs.acs.org/doi/10.1021/acs.cgd.2c00795.

Full experimental details for all compounds and computational details, including NMR and IR spectral data, TG curves, PXRD patterns, and variable-temperature single-crystal diffraction data (PDF)

Accession Codes

CCDC 2181974, 2181976−2181977, 2181980−2181989, 2182178, 2182311, 2182459, 2182640, 2182780, and 2207551 contain the supplementary crystallographic data for this paper. These data can be obtained free of charge via www.ccdc.cam.ac.uk/data_request/cif, or by emailing data_request@ccdc.cam.ac.uk, or by contacting The Cambridge Crystallographic Data Centre, 12 Union Road, Cambridge CB2 1EZ, UK; fax: +44 1223 336033.

■ AUTHOR INFORMATION

Corresponding Authors

Aaron Mailman − *Department of Chemistry, NanoScience Centre, University of Jyväskylä, FI-40014 Jyväskylä, Finland;* orcid.org/0000-0003-2067-8479; Email: aaron.m.mailman@jyu.fi

Heikki M. Tuononen − *Department of Chemistry, NanoScience Centre, University of Jyväskylä, FI-40014 Jyväskylä, Finland;* orcid.org/0000-0002-4820-979X; Email: heikki.m.tuononen@jyu.fi

Rodolphe Clérac − *Univ. Bordeaux, CNRS, Centre de Recherche Paul Pascal (CRPP), UMR 5031, 33600 Pessac, France;* orcid.org/0000-0001-5429-7418; Email: rodolphe.clerac@u-bordeaux.fr

Authors

Anni I. Taponen − *Department of Chemistry, NanoScience Centre, University of Jyväskylä, FI-40014 Jyväskylä, Finland*

Awatef Ayadi − *Department of Chemistry, NanoScience Centre, University of Jyväskylä, FI-40014 Jyväskylä, Finland*

Noora Svahn − *Department of Chemistry, NanoScience Centre, University of Jyväskylä, FI-40014 Jyväskylä, Finland*

Manu K. Lahtinen − *Department of Chemistry, NanoScience Centre, University of Jyväskylä, FI-40014 Jyväskylä, Finland;* orcid.org/0000-0001-5561-3259

Mathieu Rouzières − *Univ. Bordeaux, CNRS, Centre de Recherche Paul Pascal (CRPP), UMR 5031, 33600 Pessac, France;* orcid.org/0000-0003-3457-3133

Complete contact information is available at: https://pubs.acs.org/10.1021/acs.cgd.2c00795

Funding

This research was supported by the Academy of Finland under projects 333565, 336456, and 289172.

Notes

The authors declare no competing financial interest.

■ ACKNOWLEDGMENTS

The authors gratefully acknowledge Elina Hautakangas for assistance with elemental analysis, and A.M. and H.M.T. thank the Academy of Finland and the University of Jyväskylä, Department of Chemistry and NanoScience Centre for financial support. R.C. and M.R. received funding from the University of Bordeaux, the Region Nouvelle Aquitaine, Quantum Matter Bordeaux, and the Centre National de la Recherche Scientifique (CNRS).

■ REFERENCES

(1) Ferraris, J.; Cowan, D. O.; Walatka, V.; Perlstein, J. H. Electron Transfer in a New Highly Conducting Donor-Acceptor Complex. *J. Am. Chem. Soc.* **1973**, *95*, 948−949.

(2) Alves, H.; Molinari, A. S.; Xie, H.; Morpurgo, A. F. Metallic Conduction at Organic Charge-Transfer Interfaces. *Nat. Mater.* **2008**, *7*, 574−580.

(3) Wu, L.; Wu, F.; Sun, Q.; Shi, J.; Xie, A.; Zhu, X.; Dong, W. A TTF−TCNQ Complex: An Organic Charge-Transfer System with Extraordinary Electromagnetic Response Behavior. *J. Mater. Chem. C* **2021**, *9*, 3316−3323.

(4) Tomkiewicz, Y.; Taranko, A. R.; Torrance, J. B. Roles of the Donor and Acceptor Chains in the Metal-Insulator Transition in TTF-TCNQ (Tetrathiafulvalene Tetracyanoquinodimethane). *Phys. Rev. Lett.* **1976**, *36*, 751−754.

(5) Melby, L. R. Substituted Quinodimethans: VIII. Salts Derived from the 7,7,8,8-Tetracyanoquinodimethan Anion-Radical and Benzologues of Quaternary Pyrazinium Cations. *Can. J. Chem.* **1965**, *43*, 1448−1453.

(6) Fritchie, C. J. The Crystal Structure of N-Methylphenazinium Tetracyanoquinodimethanide. *Acta Crystallogr.* **1966**, *20*, 892−898.

(7) Huang, J.; Kingsbury, S.; Kertesz, M. Crystal Packing of TCNQ Anion π -Radicals Governed by Intermolecular Covalent $\pi - \pi$ Bonding: DFT Calculations and Statistical Analysis of Crystal Structures. *Phys. Chem. Chem. Phys.* **2008**, *10*, 2625−2635.

(8) Gundel, D.; Sixl, H.; Metzger, R. M.; Heimer, N. E.; Harms, R. H.; Keller, H. J.; Nöthe, D.; Wehe, D. Crystal and Molecular Structure and EPR Triplet Spin Excitons of NBP TCNQ, the 1:1 Salt of 5-(1-butyl) Phenazinium (NBP) with 2,2′- (2,5-cyclohexadiene-1,4-diylidene)-bispropanedinitrile (TCNQ). *J. Chem. Phys.* **1983**, *79*, 3678−3688.

(9) Hoffmann, S. K.; Corvan, P. J.; Singh, P.; Sethulekshmi, C. N.; Metzger, R. M.; Hatfield, W. E. Crystal Structure and Excited Triplet-State Electron Paramagnetic Resonance of the σ-Bonded TCNQ Dimer in Bis(2,9-Dimethyl-1,10-Phenanthroline) Copper(I) Tetracyanoquinodimethane Dimer $[Cu(DMP)_2]_2[TCNQ]_2$. *J. Am. Chem. Soc.* **1983**, *105*, 4608−4617.

(10) Radhakrishnan, T. P.; Van Engen, D.; Soos, Z. G. Diamagnetic to Paramagnetic Transition in Trisdimethylaminocyclopropenium Tetracyanoquinodimethanide (TDAC-TCNQ). *Mol. Cryst. Liq. Cryst. Incorporating Nonlinear Opt.* **1987**, *150*, 473−492.

(11) Dong, V.; Endres, H.; Keller, H. J.; Moroni, W.; Nöthe, D. Dimerization of 7,7,8,8-Tetracyanoquinodimethane (TCNQ) Radical Anions via σ-Bond Formation: Crystal Structure and EPR Properties of Bis(Dipyridyl)Platinum(II)−TCNQ, $[Pt(2,2'\text{-Dipy})_2^{2+}(TCNQ)_2^{2-}]$. *Acta Crystallogr., Sect. B: Struct. Crystallogr. Cryst. Chem.* **1977**, *33*, 2428−2431.

(12) Černák, J.; Kuchár, J.; Hegedüs, M. Disorder of the Dimeric TCNQ−TCNQ Unit in the Crystal Structure of $[Ni(Bpy)_3]_2(TCNQ{-}TCNQ)(TCNQ)_2{\cdot}6H_2O$ (TCNQ is 7,7,8,8-Tetra-

https://doi.org/10.1021/acs.cgd.2c00795
Cryst. Growth Des. XXXX, XXX, XXX−XXX

cyanoquinodimethane). *Acta Crystallogr., Sect. E: Crystallogr. Commun.* **2017**, *73*, 8−12.
(13) Shimomura, S.; Horike, S.; Matsuda, R.; Kitagawa, S. Guest-Specific Function of a Flexible Undulating Channel in a 7,7,8,8-Tetracyano-*p*-Quinodimethane Dimer-Based Porous Coordination Polymer. *J. Am. Chem. Soc.* **2007**, *129*, 10990−10991.
(14) Shimomura, S.; Higuchi, M.; Matsuda, R.; Yoneda, K.; Hijikata, Y.; Kubota, Y.; Mita, Y.; Kim, J.; Takata, M.; Kitagawa, S. Selective Sorption of Oxygen and Nitric Oxide by an Electron-Donating Flexible Porous Coordination Polymer. *Nat. Chem.* **2010**, *2*, 633−637.
(15) Zhao, H.; Heintz, R. A.; Ouyang, X.; Dunbar, K. R.; Campana, C. F.; Rogers, R. D. Spectroscopic, Thermal, and Magnetic Properties of Metal/TCNQ Network Polymers with Extensive Supramolecular Interactions between Layers. *Chem. Mater.* **1999**, *11*, 736−746.
(16) Kim, J.; Silakov, A.; Yennawar, H. P.; Lear, B. J. Structural, Electronic, and Magnetic Characterization of a Dinuclear Zinc Complex Containing $TCNQ^{-}$ and a μ-$[TCNQ–TCNQ]^{2-}$ Ligand. *Inorg. Chem.* **2015**, *54*, 6072−6074.
(17) Černák, J.; Hegedüs, M.; Váhovská, L.; Kuchár, J.; Šoltésová, D.; Čižmár, E.; Feher, A.; Falvello, L. R. Syntheses, Crystal Structures and Magnetic Properties of Complexes Based on $[Ni(L\text{-}L)_3]^{2+}$ Complex Cations with Dimethylderivatives of 2,2′-Bipyridine and TCNQ. *Solid State Sci.* **2018**, *77*, 27−36.
(18) Mikami, S.; Sugiura, K.; Miller, J. S.; Sakata, Y. Two-Dimensional Honeycomb Network Formed by Porphyrinatomanganese(III) and μ_4-σ-Dimerized 7,7,8,8-Tetracyano-*p*-Quinodimethane Dianion. *Chem. Lett.* **1999**, *28*, 413−414.
(19) Zhao, H.; Heintz, R. A.; Dunbar, K. R.; Rogers, R. D. Unprecedented Two-Dimensional Polymers of Mn(II) with $TCNQ^{\cdot-}$ (TCNQ = 7,7,8,8-Tetracyanoquinodimethane). *J. Am. Chem. Soc.* **1996**, *118*, 12844−12845.
(20) Karadas, F.; Avendano, C.; Hilfiger, M. G.; Prosvirin, A. V.; Dunbar, K. R. Use of a Rhenium Cyanide Nanomagnet as a Building Block for New Clusters and Extended Networks. *Dalton Trans.* **2010**, *39*, 4968−4977.
(21) Morosin, B.; Plastas, H. J.; Coleman, L. B.; Stewart, J. M. The Crystal Structure of the Charge-Transfer Complex between N-Ethylphenazinium (EtP) and Dimerized 7,7,8,8-Tetracyanoquinodimethanide (TCNQ) Ions, $(C_{14}H_{13}N_2)_2{\cdot}C_{24}H_8N_8$. *Acta Crystallogr., Sect. B: Struct. Crystallogr. Cryst. Chem.* **1978**, *34*, 540−543.
(22) Koivisto, B. D.; Hicks, R. G. The Magnetochemistry of Verdazyl Radical-Based Materials. *Coord. Chem. Rev.* **2005**, *249*, 2612−2630.
(23) Mukai, K.; Jinno, S.; Shimobe, Y.; Azuma, N.; Taniguchi, M.; Misaki, Y.; Tanaka, K.; Inoue, K.; Hosokoshi, Y. Genuine Organic Magnetic Semiconductors: Electrical and Magnetic Properties of the TCNQ and Iodide Salts of Methylpyridinium-Substituted Verdazyl Radicals. *J. Mater. Chem.* **2003**, *13*, 1614−1621.
(24) Taponen, A. I.; Ayadi, A.; Lahtinen, M. K.; Oyarzabal, I.; Bonhommeau, S.; Rouzières, M.; Mathonière, C.; Tuononen, H. M.; Clérac, R.; Mailman, A. Room-Temperature Magnetic Bistability in a Salt of Organic Radical Ions. *J. Am. Chem. Soc.* **2021**, *143*, 15912−15917.
(25) CrysAlisPRO, Oxford Diffraction /Agilent Technologies UK Ltd, Yarnton, England.
(26) Sheldrick, G. M. *SHELXT* − Integrated space-group and crystal-structure determination. *Acta Crystallogr., Sect. A: Found. Adv.* **2015**, *71*, 3−8.
(27) Dolomanov, O. V.; Bourhis, L. J.; Gildea, R. J.; Howard, J. A. K.; Puschmann, H. *OLEX2*: a complete structure solution, refinement and analysis Program. *J. Appl. Crystallogr.* **2009**, *42*, 339−341.
(28) Gruene, T.; Hahn, H. W.; Luebben, A. V.; Meilleur, F.; Sheldrick, G. M. Refinement of macromolecular structures against neutron data with *SHELXL2013*. *J. Appl. Crystallogr.* **2014**, *47*, 462−466.
(29) Degen, T.; Sadki, M.; Bron, E.; König, U.; Nénert, G. The HighScore Suite. *Powder Diffr.* **2014**, *29*, S13−S18.
(30) Pawley, G. S. Unit-Cell Refinement from Powder Diffraction Scans. *J. Appl. Crystallogr.* **1981**, *14*, 357−361.
(31) Grimme, S.; Ehrlich, S.; Goerigk, L. Effect of the Damping Function in Dispersion Corrected Density Functional Theory. *J. Comput. Chem.* **2011**, *32*, 1456−1465.
(32) Grimme, S.; Antony, J.; Ehrlich, S.; Krieg, H. A Consistent and Accurate Ab Initio Parametrization of Density Functional Dispersion Correction (DFT-D) for the 94 Elements H-Pu. *J. Chem. Phys.* **2010**, *132*, 154104.
(33) Adamo, C.; Barone, V. Toward Reliable Density Functional Methods without Adjustable Parameters: The PBE0 Model. *J. Chem. Phys.* **1999**, *110*, 6158−6170.
(34) Ernzerhof, M.; Scuseria, G. E. Assessment of the Perdew−Burke−Ernzerhof Exchange-Correlation Functional. *J. Chem. Phys.* **1999**, *110*, 5029−5036.
(35) Perdew, J. P.; Burke, K.; Ernzerhof, M. Generalized Gradient Approximation Made Simple [Phys. Rev. Lett. 77, 3865 (1996)]. *Phys. Rev. Lett.* **1997**, *78*, 1396.
(36) Perdew, J. P.; Burke, K.; Ernzerhof, M. Generalized Gradient Approximation Made Simple. *Phys. Rev. Lett.* **1996**, *77*, 3865−3868.
(37) Vydrov, O. A.; Scuseria, G. E.; Perdew, J. P. Tests of Functionals for Systems with Fractional Electron Number. *J. Chem. Phys.* **2007**, *126*, 154109.
(38) Vydrov, O. A.; Scuseria, G. E. Assessment of a Long-Range Corrected Hybrid Functional. *J. Chem. Phys.* **2006**, *125*, 234109.
(39) Vydrov, O. A.; Heyd, J.; Krukau, A. V.; Scuseria, G. E. Importance of Short-Range versus Long-Range Hartree-Fock Exchange for the Performance of Hybrid Density Functionals. *J. Chem. Phys.* **2006**, *125*, 074106.
(40) Henderson, T. M.; Izmaylov, A. F.; Scalmani, G.; Scuseria, G. E. Can Short-Range Hybrids Describe Long-Range-Dependent Properties? *J. Chem. Phys.* **2009**, *131*, 044108.
(41) Weigend, F.; Ahlrichs, R. Balanced Basis Sets of Split Valence, Triple Zeta Valence and Quadruple Zeta Valence Quality for H to Rn: Design and Assessment of Accuracy. *Phys. Chem. Chem. Phys.* **2005**, *7*, 3297−3305.
(42) Throughout the rest of the text, the abbreviations DTDA/DSDA and TCNQ refer to the radical-cations and -anions, respectively, without explicitly specifying the charge or the unpaired electron.
(43) Taponen, A. I.; Wong, J. W. L.; Lekin, K.; Assoud, A.; Robertson, C. M.; Lahtinen, M.; Clérac, R.; Tuononen, H. M.; Mailman, A.; Oakley, R. T. Non-Innocent Base Properties of 3- and 4-Pyridyl-Dithia- and Diselenadiazolyl Radicals: The Effect of N -Methylation. *Inorg. Chem.* **2018**, *57*, 13901−13911.
(44) Aubert, C.; Bégué, J.-P. A Simple Preparation of Alkyl Trifluoromethanesulfonates (Triflates) from Alkyl Trimethylsilyl Ethers. *Synthesis* **1985**, *1985*, 759−760.
(45) Lamoureux, M.; Milne, J. The Disproportionation of Diselenium Dichloride, Se_2Cl_2, and Diselenium Dibromide, Se_2Br_2. *Can. J. Chem.* **1989**, *67*, 1936−1941.
(46) Schelter, E. J.; Morris, D. E.; Scott, B. L.; Thompson, J. D.; Kiplinger, J. L. Toward Actinide Molecular Magnetic Materials: Coordination Polymers of U(IV) and the Organic Acceptors TCNQ and TCNE. *Inorg. Chem.* **2007**, *46*, 5528−5536.
(47) Groom, C. R.; Bruno, I. J.; Lightfoot, M. P.; Ward, S. C. The Cambridge Structural Database. *Acta Crystallogr., Sect. B: Struct. Sci., Cryst. Eng. Mater.* **2016**, *72*, 171−179.
(48) Wu, J.; MacDonald, D. J.; Clérac, R.; Jeon, I.-R.; Jennings, M.; Lough, A. J.; Britten, J.; Robertson, C.; Dube, P. A.; Preuss, K. E. Metal Complexes of Bridging Neutral Radical Ligands: PymDTDA and PymDSDA. *Inorg. Chem.* **2012**, *51*, 3827−3839.
(49) Constantinides, C. P.; Eisler, D. J.; Alberola, A.; Carter, E.; Murphy, D. M.; Rawson, J. M. Weakening of the π^*−π^* Dimerisation in 1,2,3,5-Dithiadiazolyl Radicals: Structural, EPR, Magnetic and Computational Studies of Dichlorophenyl Dithiadiazolyls, $Cl_2C_6H_3CNSSN$. *CrystEngComm* **2014**, *16*, 7298−7312.
(50) Höfs, H.-U.; Bats, J. W.; Gleiter, R.; Hartmann, G.; Mews, R.; Eckert-Maksić, M.; Oberhammer, H.; Sheldrick, G. M. Perhalogenierte 1,2,3,5-Dithiadiazolium-Salze und 1,2,3,5-Dithiadiazole. *Chem. Ber.* **1985**, *118*, 3781−3804.

https://doi.org/10.1021/acs.cgd.2c00795
Cryst. Growth Des. XXXX, XXX, XXX−XXX

(51) Allen, C.; Haynes, D. A.; Pask, C. M.; Rawson, J. M. Co-Crystallisation of Thiazyl Radicals: Preparation and Crystal Structure of [PhCNSSN][C_6F_5CNSSN]. *CrystEngComm* **2009**, *11*, 2048−2050.
(52) Yan, B.; Horton, P. N.; Weston, S. C.; Russell, A. E.; Grossel, M. C. Novel TCNQ-Stacking Motifs in (12-Crown-4)-Complexes of Alkali Metal TCNQ Salts. *CrystEngComm* **2021**, *23*, 6755−6760.
(53) Melen, R. L.; Less, R. J.; Pask, C. M.; Rawson, J. M. Structural Studies of Perfluoroaryldiselenadiazolyl Radicals: Insights into Dithiadiazolyl Chemistry. *Inorg. Chem.* **2016**, *55*, 11747−11759.

https://doi.org/10.1021/acs.cgd.2c00795
Cryst. Growth Des. XXXX, XXX, XXX−XXX